

## From falling to flying: the path to powered flight of a robotic samara nano air vehicle

This content has been downloaded from IOPscience. Please scroll down to see the full text.

2010 Bioinspir. Biomim. 5 045009

(<http://iopscience.iop.org/1748-3190/5/4/045009>)

View [the table of contents for this issue](#), or go to the [journal homepage](#) for more

Download details:

IP Address: 158.130.23.8

This content was downloaded on 10/03/2015 at 18:59

Please note that [terms and conditions apply](#).

# From falling to flying: the path to powered flight of a robotic samara nano air vehicle

Evan R Ulrich, Darryll J Pines and J Sean Humbert

University of Maryland, College Park, MD 20742, USA

E-mail: [evanu@umd.edu](mailto:evanu@umd.edu)

Received 9 March 2010

Accepted for publication 8 November 2010

Published 24 November 2010

Online at [stacks.iop.org/BB/5/045009](http://stacks.iop.org/BB/5/045009)

## Abstract

This paper details the development of a nano-scale ( $>15$  cm) robotic samara, or winged seed. The design of prototypes inspired by naturally occurring geometries is presented along with a detailed experimental process which elucidates similarities between mechanical and robotic samara flight dynamics. The helical trajectories of a samara in flight were observed to differ in-flight path and descent velocity. The body roll and pitch angular rates for the differing trajectories were observed to be coupled to variations in wing pitch, and thus provide a means of control. Inspired by the flight modalities of the bio-inspired samaras, a robotic device has been created that mimics the autorotative capability of the samara, whilst providing the ability to hover, climb and translate. A high-speed camera-based motion capture system is used to observe the flight dynamics of the mechanical and robotic samara. Similarities in the flight dynamics are compared and discussed as it relates to the design of the robotic samara.

(Some figures in this article are in colour only in the electronic version)

## 1. Introduction

Samaras, or winged seeds, are the sole method by which several species of plants disperse their seed. Geometric configurations for maximal seed dispersal have evolved into two main classes of seeds [1]. Both of which execute autorotational flight as they fall from the tree, and one of which additionally rotates about its longitudinal axis. This discussion is limited to samaras which execute only autorotational flight.

The flight of rotary-winged seeds have been studied since the early 1950s. Initial experimentation sought to quantify seed dispersal characteristics for the study of population dynamics. Previous work in this field has characterized surface roughness, center of gravity placement, leading edge thickness and planform design which is detailed in [2–6]. A dynamic model was proposed by Seter and Rosen [3] that allowed prediction of terminal velocity and some in-flight characteristics based on simplifying assumptions. Wing surface characteristics and some simple geometries were studied by Azuma and Yasuda [2]. The low Reynolds number flight of the samara was shown by Lentink *et al* [7] to be similar to that found in some species of insects and birds.

A method of observing the progression of the samara's dynamics is through drop testing in a room, ideally one without ventilation, where known and repeatable initial conditions can be guaranteed. Perturbations caused by errors in the initial release of the samara are a source of uncertainty that can be reduced by increasing the initial drop height, thus giving more time for the perturbation to settle. Precise and continual observation of the samara in flight is necessary to capture the small oscillatory motion of the wing in flight. A strobing high-speed camera system is used to record the flight path of the vehicles which are fitted with retro-reflective markers.

The robotic samara vehicle detailed in this study is a type of mono-wing rotorcraft modeled after the flight of samaras, or winged seeds. The models in this work are substantially larger than most natural samara; however, larger samara does exist like the species *Centrolobium Leguminosae* that has been found to range in size from 15 to 30 cm, see Pirie *et al* [8]. The layout of the vehicle consists of two rigid bodies linked by a servo allowing one rotational degree of freedom. The first rigid body and main lifting surface resemble a scaled version of a samara both in planform geometry and airfoil cross section, detailed by Ulrich *et al* in [9–12]. The second rigid body

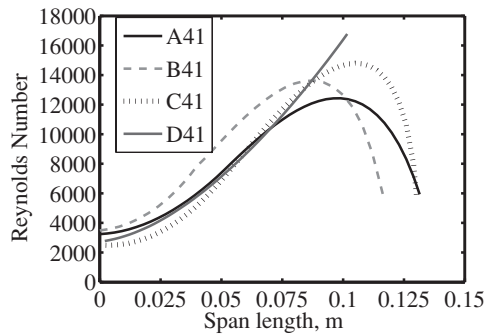


**Figure 1.** Mechanical samara Reynolds number variation with span length [10].

houses the electronics and motor/propellor unit applying a torque to rotate the vehicle as required for flight. Flight of a monocopter differs from full-scale helicopters as there exists no stationary frame of reference from which control inputs can be applied, i.e. helicopter swashplate. Control of the vehicle with once per revolution inputs requires knowledge of the vehicle's orientation relative to the desired flight path, but sensor packages capable of recording on-board flight data at the rate necessary for this type of control are not commercially available in the weight class required for use on nano-class vehicles. An approach to directional control which does not require the once per revolution actuation or high frequency measurement of vehicle orientation is discussed in detail in this paper.

This paper characterizes the key aspects of a study of the flight dynamics of powered and unpowered single-wing rotorcraft with design based on one of nature's most efficient fliers: the samara. The work begins with a description of the design of the mechanical samaras and experimental setup used to record free flight. Then the characteristics of the recorded flight paths are analyzed, and the variation in flight modalities is discussed. The following section details the aspects of robotic samara design and how control is implemented through

exploiting flight modalities observed in the autorotation of mechanical samara. Next three robotic samara designs are discussed and compared to traditional aircraft, and the unique aspects of the robotic samara rotor design are compared with full-scale helicopter rotor design. Finally, translational flight of the robotic samara is demonstrated and discussed for three different flight paths including a 180° turn.

## 2. Unpowered free-flight experiments

### 2.1. Mechanical samara design

The geometry of the models tested is not simple scaled-up versions of natural samaras. The design involved a trial and error method aimed at producing a mechanical samara capable of being tested in the limited space of the laboratory, with the main constraint being the height of the ceiling. The resulting planform and chord geometry are similar to those found in natural samaras; however, a direct comparison is not possible as the scale of the models presented here is at least an order of magnitude larger than natural samaras that have been studied previously.

Design of the mechanical samara involves precise placement of the center of mass, as a poor choice results in a less stable and efficient autorotation. First observed by Schmitz [13], the low Reynolds number flight regime of the mechanical samara (see figure 1) requires a non-standard airfoil cross-section which is based on geometric properties observed in natural samara; however, those designed for these experiments exhibit a generally smooth surface.

Each subject is designed with similar cross-sectional properties that only differ in chord length. The general layout of the airfoil includes a thick leading edge followed by a thin region that extends to the trailing edge. This distribution of mass along the chord line is required for stable autorotation. Stiffeners span the length of the samara wing and are required for structural rigidity of the model, figure 2.

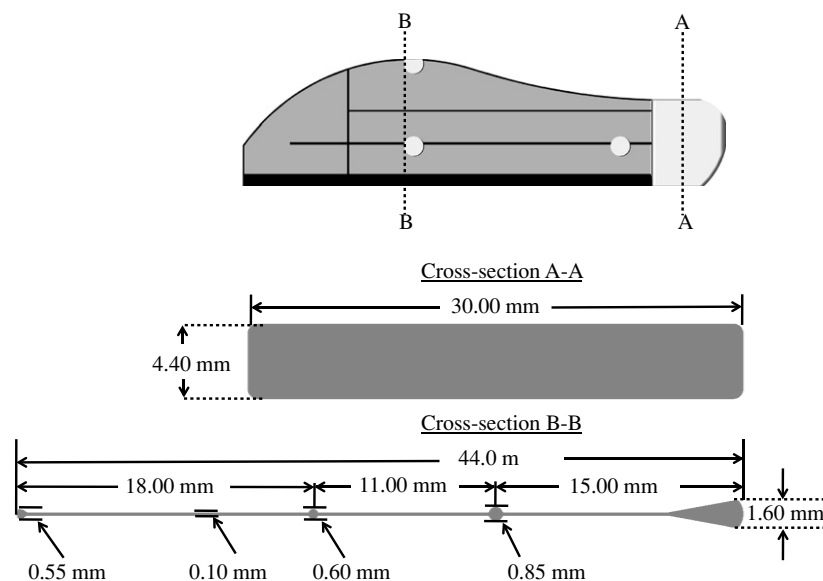


**Figure 2.** Samara model airfoil cross-section.

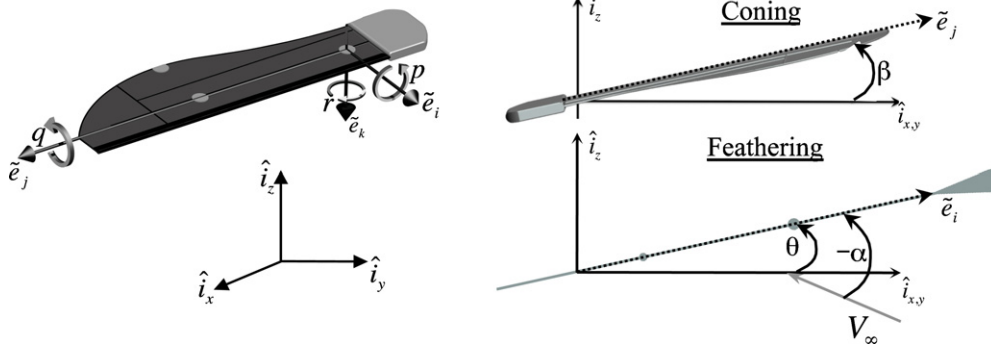


**Figure 3.** Mechanical samara orientation.

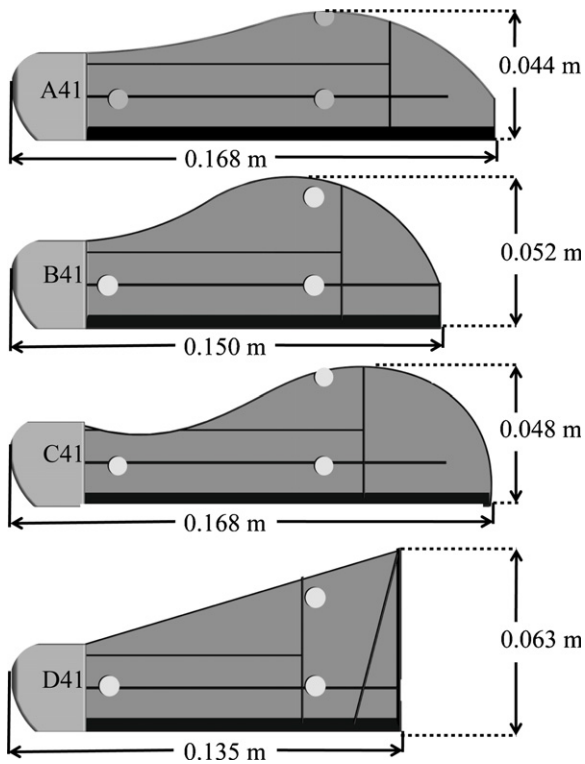


**Figure 4.** Samara model geometry, retro-reflective marker locations shown as light colored circles on the models [10].

The models were designed using CAD software capable of calculating precisely the model surface area and the location of the center of mass as well as overall model mass. These parameters are held constant over the four different subjects shown in figure 4. The four different subjects tested have the physical properties listed in tables 1, 2, and geometries shown in figure 4. All of the mechanical samaras are planar symmetric, and hence have zero twist. The inertias reported here include the final addition of the marker mass. The CAD model can then be exported as a stereo-lithography file (STL), which is a representation of the samara's geometry as approximated by triangles of varying dimension. This file is then used by the Eden350 rapid prototyping machine to create the physical prototype. The tolerances of the machine are  $42 \mu\text{m}$  in the  $XY$ -plane and  $16 \mu\text{m}$  in the  $Z$ -plane [23]. Subjects are built in the same orientation on the machine to ensure

**Table 1.** Mechanical samara material properties, VeroBlack [24].

Property	ASTM	Unit	Value
Tensile strength	D-638-03	Mpa	$5.070 \times 10^1$
Modulus of elasticity	D-638-04	Mpa	$2.192 \times 10^3$
Flexural strength	D-790-03	Mpa	$7.960 \times 10^1$
Flexural modulus	D-790-04	Mpa	$2.276 \times 10^3$
Density		$\text{Kg m}^{-3}$	1118

similarity between models. The resin type used to construct all tested mechanical samara is VeroBlack [24]. The resin was chosen for its high color contrast with the reflective markers and its material properties which are listed in table 1.

The orientation of the samara is defined by three points that are used to form the orthonormal basis set  $[\tilde{e}_x, \tilde{e}_y, \tilde{e}_z]$  that defines the body fixed velocities  $[u, v, w]$  and angular rates  $[p, q, r]$  with respect to a fixed inertial coordinate system  $[\hat{i}_x, \hat{i}_y, \hat{i}_z]$ , figure 3. The coning  $\beta$  and feathering  $\theta$  angles are defined by the orientation of the samara relative to the fixed frame, and can be seen in relation to the relative wind  $V_\infty$  and an aerodynamic angle of attack  $\alpha$  in figure 3. Additional details of this process can be found in [10].

## 2.2. Experimental setup

The flight dynamics of the samara can be measured through high-speed (350 frames per second) camera-based motion capture. This method eliminates the need for costly and fragile micro-scaled sensor packages, and is employed with use of a Vicon vision system. The system collects data by capturing 2D images of the subject which is fitted with retro-reflective markers. The Vicon system strobes light at the frame rate of the camera [25]. The light incident on the surface of the marker returns to its source, reducing errors commonly caused by interference. The light returned to the lens allows for a quick computation of the centroid of the marker. Three-dimensional position is obtained from a least-squares fit of the two-dimensional camera observations. The setup of the workspace tracked by the Vicon system is shown in figure 5 and is limited to the area labeled as the data capture region. This setup allowed the samara to fall a distance of 5 m before flight data were recorded.

A stable autorotation was achieved in every flight test observed; however, the chaotic flight prior to autorotation often

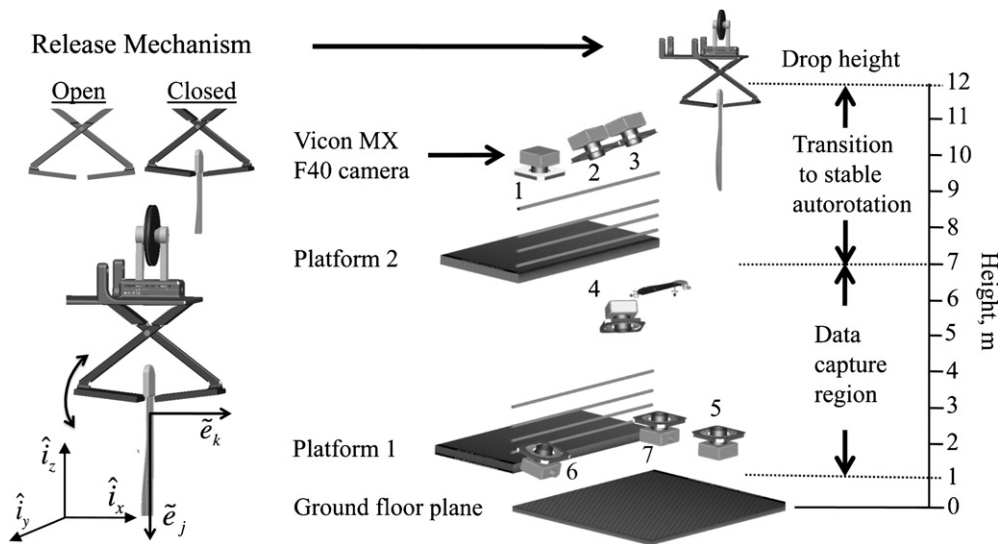


**Figure 5.** Depiction of experimental workspace.

**Table 2.** Physical properties of the mechanical samaras.

Item	Symbol	Units	A41	B41	C41	D41	Multiplier
Length of wing	$L_w$	m	0.168	0.150	0.168	0.135	
Span of wing (CG to tip)	$R$	m	0.131	0.116	0.130	0.102	
Mass	$m_w$	Kg	5.26	5.26	5.26	5.26	$\times 10^{-3}$
Total weight	$W$	N	0.052	0.052	0.052	0.052	
Surface area	$S$	m <sup>2</sup>	1.24	1.24	1.24	1.24	$\times 10^{-2}$
Max chord	$c_m$	m	0.044	0.052	0.048	0.063	
Aspect ratio	$R^2/S$	—	2.29	1.81	2.27	1.48	
Wing loading	$W/S$	Nm <sup>-2</sup>	4.16	4.16	4.16	4.16	
Disk loading	$W/\pi R^2$	0.96	1.23	0.98	1.59		
Principal	$I_1$	Kg m <sup>2</sup>	4.99	5.80	5.16	6.59	$\times 10^{-7}$
Moments of inertia	$I_2$	Kg m <sup>2</sup>	9.64	7.62	10.0	7.6	$\times 10^{-6}$
	$I_3$	Kg m <sup>2</sup>	10.1	8.18	10.5	8.29	$\times 10^{-6}$
Rotation angle:							
$[\tilde{e}_x]$ to $I_1$	—	Degree	0	0	0	0	
$[\tilde{e}_y]$ to $I_2$	—	Degree	0	0	0	0	
$[\tilde{e}_z]$ to $I_3$	—	Degree	88.348	89.964	89.354	93.439	
Radius of gyration	$R_1$	mm	9.74	10.50	9.90	11.12	
	$R_2$	mm	42.81	38.04	43.58	37.82	
	$R_3$	mm	43.87	39.42	44.66	39.38	

resulted in the samara traveling outside the capture volume. Two dominant flight patterns emerged which differed both in descent velocity and radius of precession. The flight path characterized by a larger radius of precession is discussed in [9], and flight path characterized by a smaller radius of precession is discussed in [10].

A simple mechanical release mechanism is used to hold the samara so that the span of the wing  $\tilde{e}_y$  points in the  $\hat{i}_z$  direction. The grip on the release mechanism is grooved to help align the samara for each drop test. The mechanical samara has no grooves and is held at the location where the chord changes from 4.4 to 1.4 mm in thickness. The repeatability of the release was verified visually and was observed to consistently and symmetrically deploy the samara. This release mechanism is mounted 12 m above the ground, and is released after transient motion has been eliminated

with the physical contact the mechanism makes with the platform mounted to the ceiling. The samara is placed into the gripper, and hoisted to the ceiling by an attached thread of monofilament, which drapes over a pulley and back down to the ground, where it is attached to a fishing rod.

In order to minimize wind disturbances which may effect the flight dynamics, these experiments were conducted in a room which had no ventilation. The flow properties of the room were not measured and were assumed to be uniform across the range of subjects tested. The test facility encompassed two platforms which provided the area for camera placement. The viewing angle of the cameras is critical in capture as well as calibration of the system. A minimum of three cameras are needed to calibrate the ground plane. This step in the calibration dictates the skew, if any, of the vertical axis with respect to the ground plane.

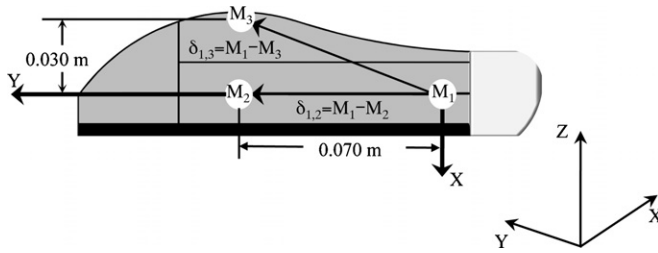


**Figure 6.** Retro-reflective marker placement (Vicon body fixed coordinate frame) [10].

**Table 3.** Measurement characteristics.

Measurement	Symbol	Variance	Unit
Time	$t$	—	s
Position	$x, y, z$	$0.6128 \times 10^{-3}$	m
Orientation	$\phi, \theta, \psi$	$7.8000 \times 10^{-3}$	rad
Translational velocity	$u, v, w$	$0.2510 \times 10^{-3}$	$\text{m s}^{-1}$
Rotational velocity	$p, q, r$	$1.2000 \times 10^{-3}$	$\text{rad s}^{-1}$

To avoid potential pitfalls from a poorly calibrated ground plane, markers are distributed in the area of interest, and the Vicon system takes an average of the location of the markers which enhances the previously calibrated ground plane. This calibration gives the user a least-squares estimate of the error associated with the tracking of each marker. Tracking errors for the trials included here were measured by recording data while the mechanical samara was motionless. The resultant measurement characteristics are displayed in table 3.

The location of the markers placed on the subjects is recorded by the Vicon system prior to flight testing. This calibration aids in the proper labeling of reconstructed marker location by excluding erroneous data that fall outside of the possible range of marker location for a given subject. The subjects are designed with circular grooves which trace the outline of the intended marker location enabling precise placement of the retro-reflective tape. Any error in the marker location is reduced in the calibration of the samara to the values reported in table 3. Typical motion capture work employs spherical marker geometry. In this work, a flat circular marker that is 0.007 m in diameter and 0.0001 m in thickness is used.

The non-standard marker geometry is chosen to interfere minimally with the aerodynamics of the samaras tested. A marker is placed in the same location on both sides of a samara and represents a single-marker location to the visual tracking system. The conformal markers are intentionally placed on the samara in locations that are raised from the surface. This provides the marker with some three dimensionality which aids in the ability of the vision system to track a samara. The marker disks were made using a hole punch on 3M 7610 high-gain reflective sheeting. Three markers are placed on the samara permitting attitude determination. Marker placement for the rigid body model is shown in figure 6 in Vicon inertial coordinates. A representative schematic showing the virtual flight path of the samara as observed by the vision system is shown in figure 7. The unprocessed flight data for each of the models, as recorded by Vicon, are shown in figure 8.

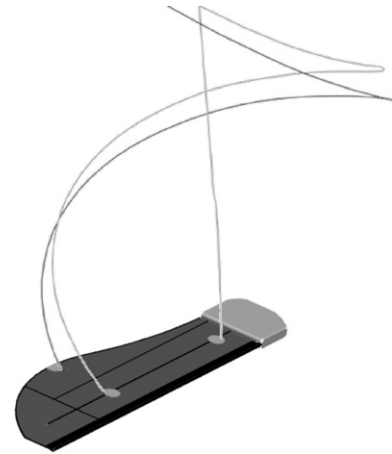


**Figure 7.** Virtual flight path [10].

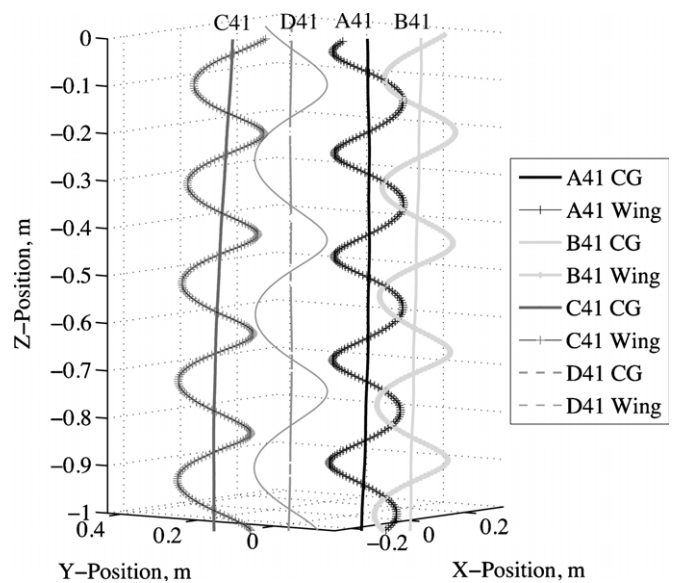


**Figure 8.** Mechanical samara flight path [10].

When working with the Vicon software, a rigid body model that defines the degrees of freedom of each of the segments of the samara is required. This helps to ensure that only physically possible solutions are converged upon in the post processing of a trial. A rigid body is defined with a fixed body coordinate system; hence, the Euler angles for a clockwise descent are different than those of a counterclockwise descent. An additional rotation of  $\pi$  about the fixed body X-axis is necessary to avoid the singularity this introduces in the calculation of the orientation.

### 3. Data reduction and analysis

#### 3.1. Attitude determination

The 3D marker position data provide a means of resolving the orientation of the mechanical samara in space. The three markers are sufficient to describe an orthonormal basis from which the rotation matrix representing the samara's orientation can be formed. The first vector forms the  $\tilde{e}_j$ -axis in body frame



coordinates and is the line from the samara center of mass to the marker located 0.070 m in the positive Vicon  $Y$ -direction. The remaining bases require an intermediate vector from which to compute a cross product defining the  $\tilde{e}_k$ -axis as follows:

$$\delta_{1,2} = M_1 - M_2 \quad (1)$$

$$\delta_{1,3} = M_1 - M_3 \quad (2)$$

$$v = \frac{\delta_{1,3}}{\|\delta_{1,3}\|}. \quad (3)$$

A schematic detailing the construction of the vectors is shown in figure 6. The intermediate vector  $\delta_{1,2}$  can be normalized forming the  $\tilde{e}_i$  body frame axis. The vector  $v$  is formed by normalizing  $\delta_{1,3}$ ; this vector is then used to compute the  $\tilde{e}_k$  body frame axis. The final body axis is formed in the cross product of  $\tilde{e}_k$  and  $\tilde{e}_i$ . This set forms the orthonormal basis defining the orientation of the body with respect to the inertial frame:

$$\tilde{e}_i = \frac{\delta_{1,2}}{\|\delta_{1,2}\|} = \alpha_{11} + \alpha_{21} + \alpha_{31} \quad (4)$$

$$\tilde{e}_j = \tilde{e}_k \times \tilde{e}_i = \alpha_{12} + \alpha_{22} + \alpha_{32} \quad (5)$$

$$\tilde{e}_k = v \times \tilde{e}_i = \alpha_{13} + \alpha_{23} + \alpha_{33}. \quad (6)$$

Once the three-dimensional marker position is obtained and the basis set of the samara body axes is computed, the Euler angles can be deduced from the basis  $[\tilde{e}_i, \tilde{e}_j, \tilde{e}_k]$ . The Euler angles provide a non-unique set of rotations that describe the samara's orientation; however, a singularity arises at  $\pi/2$ . Away from the singularity, the angles are as follows:

$$\theta = \arcsin -\alpha_{13} \quad (7)$$

$$\psi = \arctan \frac{\alpha_{11}}{\alpha_{12}} \quad (8)$$

$$\phi = \arctan \frac{\alpha_{23}}{\alpha_{33}}. \quad (9)$$

To maintain continuity of signs between successive time steps near the singularity, it is necessary to set  $\psi = 0$  and compute the final angle  $\phi$  as

$$\phi = \arctan \frac{\alpha_{21}}{\alpha_{31}}. \quad (10)$$

### 3.2. Attitude representation

Subsequent testing of the various samaras provided insight into the governing dynamics as they varied with samara geometry. Attitude representation requires separate bases for the fixed inertial axes ( $F$ ) and the body axes which are fixed to the samara ( $B$ ):

$$F = [\hat{f}_x, \hat{f}_y, \hat{f}_z] \quad (11)$$

$$B = [\tilde{e}_i, \tilde{e}_j, \tilde{e}_k] \quad (12)$$

$$[\vec{r}]_B = R_1(\phi) \cdot R_2(\theta) \cdot R_3(\psi) \cdot [\vec{r}]_F. \quad (13)$$

A schematic detailing the axis of these rotations is shown in figure 3. The transformation from the inertial frame to the body frame is described by three Euler angles. The order of rotation

**Table 4.** Flight performance metrics.

Metric	$r_{CG}$ (m)	$\sigma_{r_{CG}}$ (m)	$\dot{z}_{CG}$ m s <sup>-1</sup>	$\sigma_{\dot{z}_{CG}}$ m s <sup>-1</sup>	$Y_c$ (m)
A41	0.07	0.01	-1.60	0.01	$64.60 \times 10^{-3}$
B41	0.16	0.01	-1.70	0.02	$59.00 \times 10^{-3}$
C41	0.03	0.01	-1.50	0.06	$69.80 \times 10^{-3}$
D41	0.40	0.02	-1.80	0.05	$56.20 \times 10^{-3}$

is as follows: a yaw rotation  $\psi$  about the  $\hat{f}_z$  axis, followed by a pitch rotation  $\theta$  about the new  $\hat{f}_y$  axis, and lastly a coning rotation  $\phi$  about the new  $\hat{f}_x$  axis. This rotation sequence is standard for aircraft [19]. Rotations in the fixed body frame ( $B$ ) are orthogonally projected onto the inertial frame ( $F$ ), which requires the body angular rates to be defined separately. The sum of the inner products of each of the inertial angular rates with the body axis of interest yields the body angular rates:

$$p = -\dot{\psi} \sin \theta + \dot{\phi} \quad (14)$$

$$q = \dot{\psi} \cos \theta \sin \phi + \dot{\theta} \cos \phi \quad (15)$$

$$r = \dot{\psi} \cos \theta \cos \phi - \dot{\theta} \sin \phi. \quad (16)$$

The tabulated data shown in table 4 identify key performance parameters, namely the resulting geometry for minimal descent velocity. The samara models rotate about the center of mass or CG, resulting in the majority of the wing area being located on one side of the CG, as shown in the inset in figure 17. The distance of the area centroid of this portion of the samaras is calculated with respect to the CG, and is called  $Y_c$  and quantified in table 4.

### 3.3. Flight dynamics analysis

In applications involving periodic signals it is desirable to enhance signal-to-noise ratios in order to extract representative waveforms. Time synchronous averaging (TSA) techniques previously implemented in applications such as structural health monitoring are employed here as a means of reducing a periodic signal into one discernable waveform [26, 27]. For a deterministic signal  $\chi(t)$  of period  $T$ , a measurement model can be written as

$$\kappa(t) = \chi(t) + v(t) \quad (17)$$

where  $v$  is additive sensor noise. For  $\chi(t)$  measured over  $N$  periods, the ensemble average and ensemble variance can be approximated as

$$\eta_\kappa(t) = \frac{1}{N} \sum_{n=0}^{N-1} \kappa(t + nT) \quad (18)$$

$$\sigma_\kappa^2(t) = \frac{1}{N} \sum_{n=0}^{N-1} [\kappa(t + nT) - \eta_\kappa(t)]^2. \quad (19)$$

Confidence intervals for estimated parameters can be formulated from estimation theory [28]. The 95% confidence interval of these measurements with respect to the signal averages is approximated as

$$\kappa_{0.95}(t) = \eta_\kappa(t) \pm 1.96\sigma_\kappa(t). \quad (20)$$

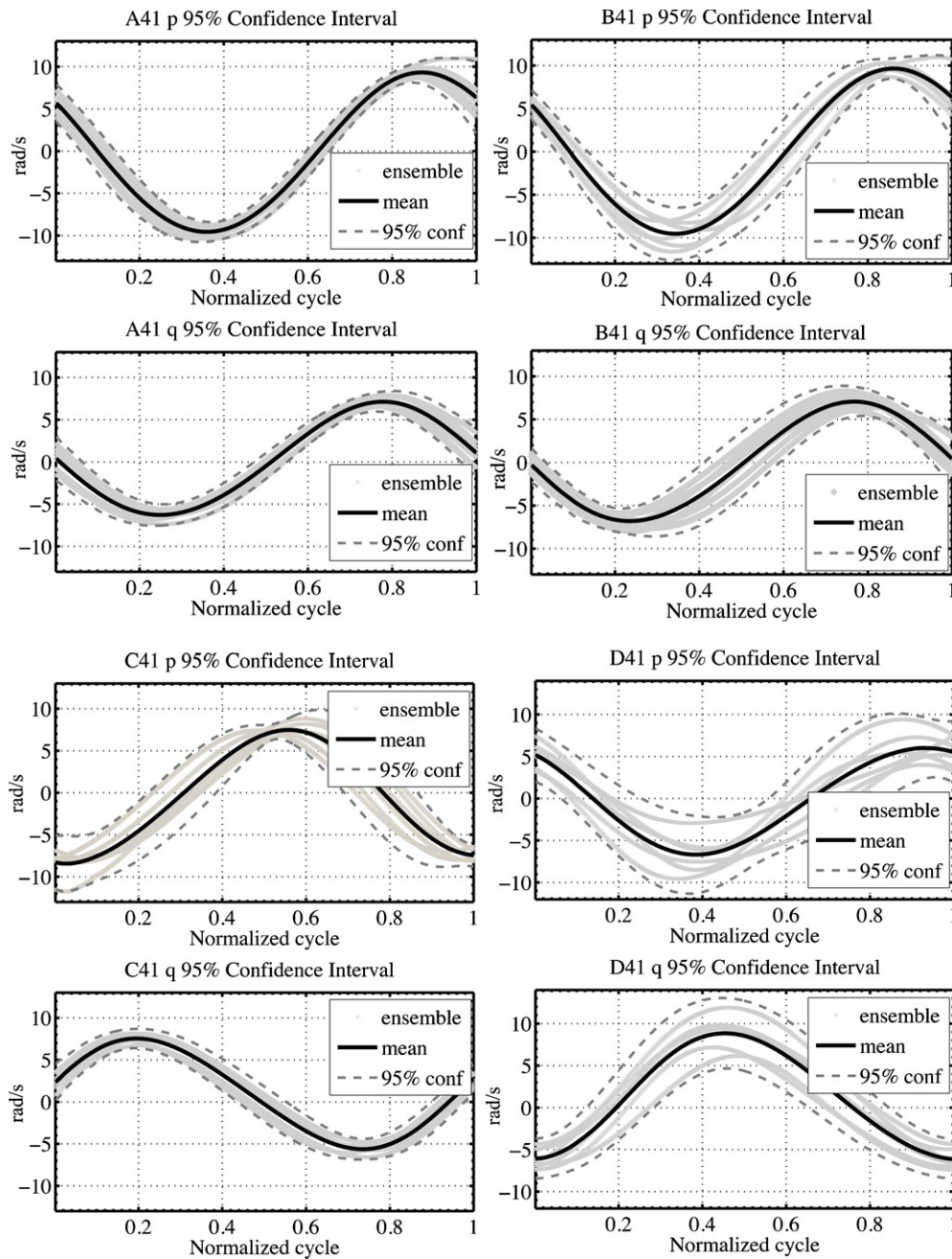


**Figure 9.** TSA flight data with 95% confidence interval [10].

This average is then described for each samara by Fourier sine or cosine series of varying order. The specific parameters used for the ensemble averaging are listed in table 5. The concatenated signals are shown in figure 9 where the gray points are the overlaid signals. The black line is the signal average with the 95% confidence interval on the upper and lower bounds. The confidence interval bounds tend to increase from samara A to D, as shown in figure 9. Possible causes for this include but are not limited to: structural vibrations, susceptibility to small wind disturbance and decreased aerodynamic damping resulting from a change in the center of pressure. The number of ensembles averaged is highly dependent on the settling time of the individual samara and the limited drop height. This number could be increased

**Table 5.** Time synchronous average parameters for each samara tested.

Model	Term	$f$ (Hz)	$T$ (s)	Points	$N$
A41	$p$	7.25	0.138	500	8
A41	$q$	7.25	0.138	500	8
B41	$p$	7.41	0.135	384	6
B41	$q$	7.41	0.135	384	6
C41	$p$	7.32	0.137	411	7
C41	$q$	7.32	0.137	411	7
D41	$p$	5.71	0.175	455	6
D41	$q$	5.71	0.175	455	6

at the cost of uncertain initial conditions by giving the samara a pre-spin upon launch.



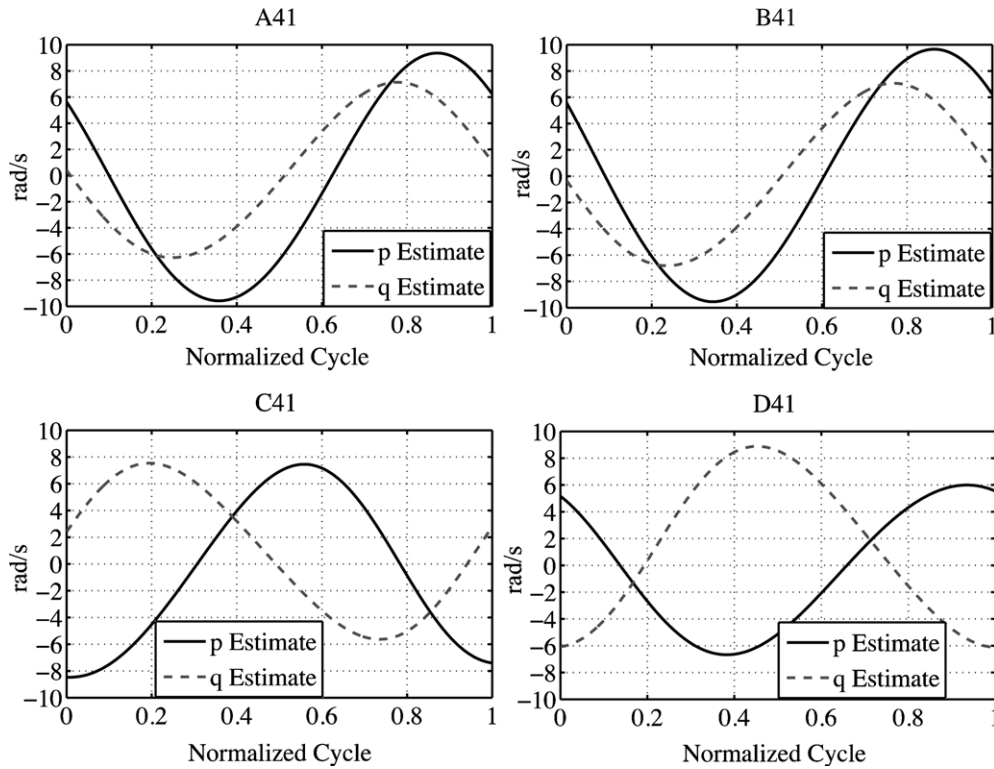


**Figure 10.** Fourier series estimation of TSA roll and pitch flight data [10].

**Table 6.** Coefficients of the Fourier series estimate of TSA roll and pitch.

State	$\omega$ rad s <sup>-1</sup>	$a_0$	$a_1$	$b_1$	$a_2$	$b_2$	$a_3$	$b_3$	MSE
$\hat{p}_A(t)$	6.206	-0.323	+5.905	-7.398	+0.049	-0.229	—	—	0.789
$\hat{q}_A(t)$	6.194	+0.257	+0.297	-6.677	-0.147	-0.240	—	—	0.024
$\hat{p}_B(t)$	2.773	-1.872	+4.004	+3.147	+3.450	-12.100	—	—	0.696
$\hat{q}_B(t)$	6.185	+0.018	-0.224	-6.912	-0.128	-0.260	—	—	0.225
$\hat{p}_C(t)$	4.059	-2.573	-4.163	+5.055	-1.399	-3.363	-0.331	+0.431	0.386
$\hat{q}_C(t)$	6.334	+0.948	+1.273	+6.392	+0.179	+0.447	—	—	0.091
$\hat{p}_D(t)$	2.947	-2.462	+0.172	+4.173	+7.113	-4.525	+0.341	-1.170	0.118
$\hat{q}_D(t)$	6.180	+1.349	-7.254	+1.627	-0.175	-0.460	—	—	0.598

The concatenated roll and pitch flight data can be represented with a Fourier series allowing a functional representation of the flight dynamics. The curve fits of the four models including the 90% confidence interval are shown in figure 10.

The most notable observation is that in steady vertical descent, roll and pitch are neither constant nor small as is required for convergence of the model derived by Seter *et al* [3, 4]. The waveform indicates a cyclic variation in the roll rate of roughly  $\pm 9.5$  rad s<sup>-1</sup> for both A41 and B41, whereas C41 varies by  $\pm 7.5$  rad s<sup>-1</sup> and D41 varies from  $-8$  to  $7.5$  rad s<sup>-1</sup>. The pitch rate observed in A41 is  $-6$  to  $7$  rad s<sup>-1</sup> and is similar in amplitude to B41 which varies by  $\pm 7$  rad s<sup>-1</sup>. The pitch rates of both C41 and D41 appear to have an offset and are not symmetric about the zero point as observed for A41 and B41. The pitch rate for C41 can be observed to vary from  $-5.5$  to  $7.5$  rad s<sup>-1</sup> and for D41 the pitch rate varies from  $-7.5$  to  $10.5$  rad s<sup>-1</sup> and exhibits a similar offset as the one observed in C41. The roll and pitch rates are represented by equations (21) and (22):

$$\hat{p}_i(t) = a_0 + \sum_{n=1}^3 [a_n \cos(\omega t) + b_n \sin(\omega t)] \quad (21)$$

$$\hat{q}_i(t) = a_0 + \sum_{n=1}^3 [a_n \cos(\omega t) + b_n \sin(\omega t)] \quad (22)$$

where  $i = [A, B, C, D]$ . The yaw rate and curve fit are neglected here as the variation in amplitude is  $2$  rad s<sup>-1</sup> or 5% of the mean, and can be approximated with the small error as a line. The resultant coefficients of the Fourier series estimate are tabulated and shown in table 6. The observed phase shift in the rotational dynamics, when measured from maximum  $p$  to maximum  $q$ , varies between the models with A41 and B41 exhibiting similar shifts of  $33.0^\circ$  and  $35.6^\circ$ , respectively. Models C41 and D41 displayed substantially larger phase shifts of  $131.7^\circ$  and  $188.7^\circ$ , respectively. One observed trend is that an increase in phase shift between  $p$  and  $q$  corresponds to an increase in the radius of precession of the center of mass,  $r_{CG}$ .

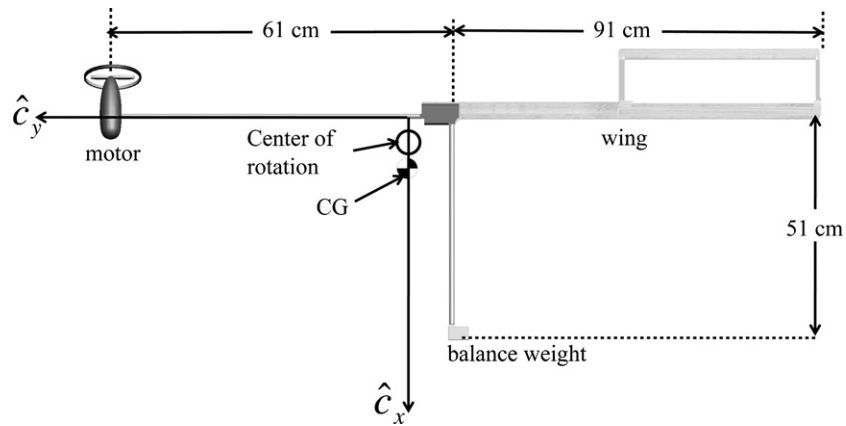


**Figure 11.** Conventional monocopter schematic, [14].

The motion observed is similar to the effect seen on a full-scale helicopter blade undergoing dynamic stall. This aerodynamic phenomenon is typically cyclic and results from the formation of a vortex that increases the local pressure, delaying stall on the airfoil. The vortex travels down the length of the chord and is shed causing a deep stall of the airfoil.

Considering the flight pattern induced by a given feathering angle, it was posited that active variation in flight could lead to changes in radius of precession similar to that observed in the two flight patterns. A prototype was created to test this concept. The wing was able to rotate with respect to a main body that contained the majority of the mass of the vehicle, as proper placement of the center of mass is required to sustain autorotation. The prototype was drop tested and was observed to qualitatively behave as expected with descent velocity, rotation rate and radius of precession, all controllable through variations in the wing pitch with respect to a main body.

#### 4. Powered flight

The concept of a single-wing rotating aircraft is not a new one, and the first vehicle of this type was flown in 1952 in the woods surrounding Lake Placid, New York by Charles W McCutchen [14]. A more recent vehicle was developed and flown by a team led by Lockheed Martin Advanced Technology Laboratories [15]. The prototype called MAVPro incorporated an outrunner motor with an 20.3 cm diameter propeller, weighed 0.514 Kg, rotated at a stable 4 Hz, and could climb to 15 m with radio-controlled actuation of a trailing edge flap. The MAVPro incorporated the AG38 airfoil, and exhibited a rectangular planform geometry. The various single-winged rotating aircraft developed over the years have made no attempt to utilize the most basic mode of transit of natural samara, autorotation [14, 15].

##### 4.1. Monocopter description

Conventional monocopter designs apply torque to the vehicle with a thrust device slightly offset from the  $\hat{c}_y$ -axis, (see figure 11) and in the case of MAVPro the propeller spins

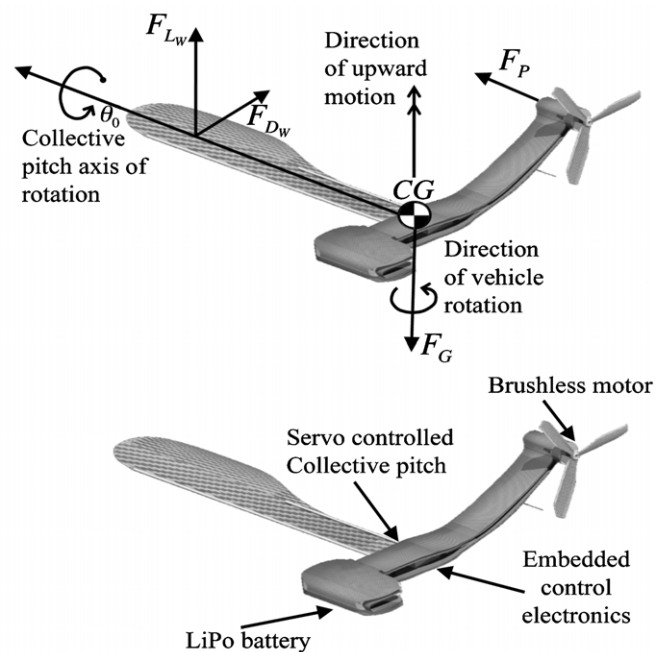


**Figure 12.** Robotic samara component and free body diagram, [11].

in the  $\hat{c}_y$ - $\hat{c}_z$  plane and influences the stability about the  $\hat{c}_y$ -axis. The 8.9 cm diameter propeller of the samara-I, II is spinning in the  $\hat{c}_x$ - $\hat{c}_z$  plane and opposes applied torque about the  $\hat{c}_x$ -axis providing additional roll stability. The configuration of samara-I, II permits control of the rotation rate, altitude and translation via the appropriate actuation of the wing servo. The component layout and free body diagram of the vehicle used in this study are shown in figure 12. The sign convention and corresponding vehicle orientation are shown in figure 13.

The authors' intent in the design of the vehicles discussed herein was to emulate the natural flight dynamics of samara, and in doing so take advantage of the highly efficient autorotation which it employs. As such, robotic samara-I, II, III use samara-inspired planform geometry and airfoil cross-sections developed previously by the authors, figure 15. These vehicles perform stable autorotation and are capable of landing at terminal velocity without sustaining any damage. In the

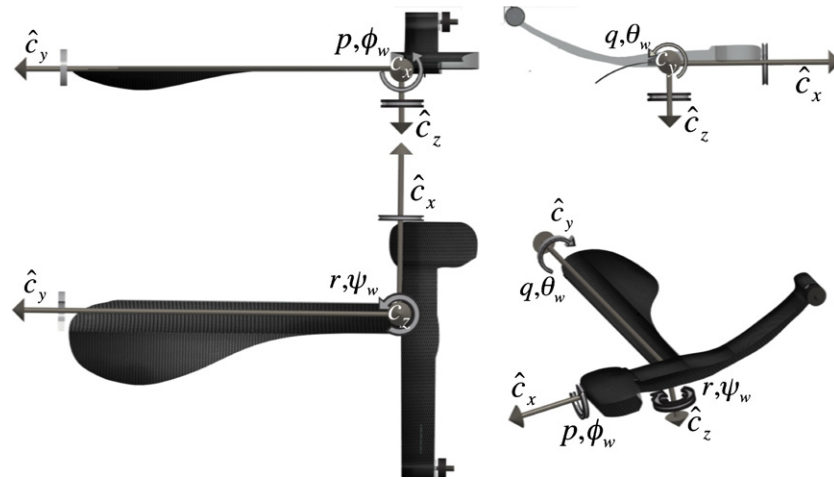


**Figure 13.** Roll ( $p$ ), pitch ( $q$ ) and yaw ( $r$ ) definitions for a fixed body coordinate system (**B**), [11].

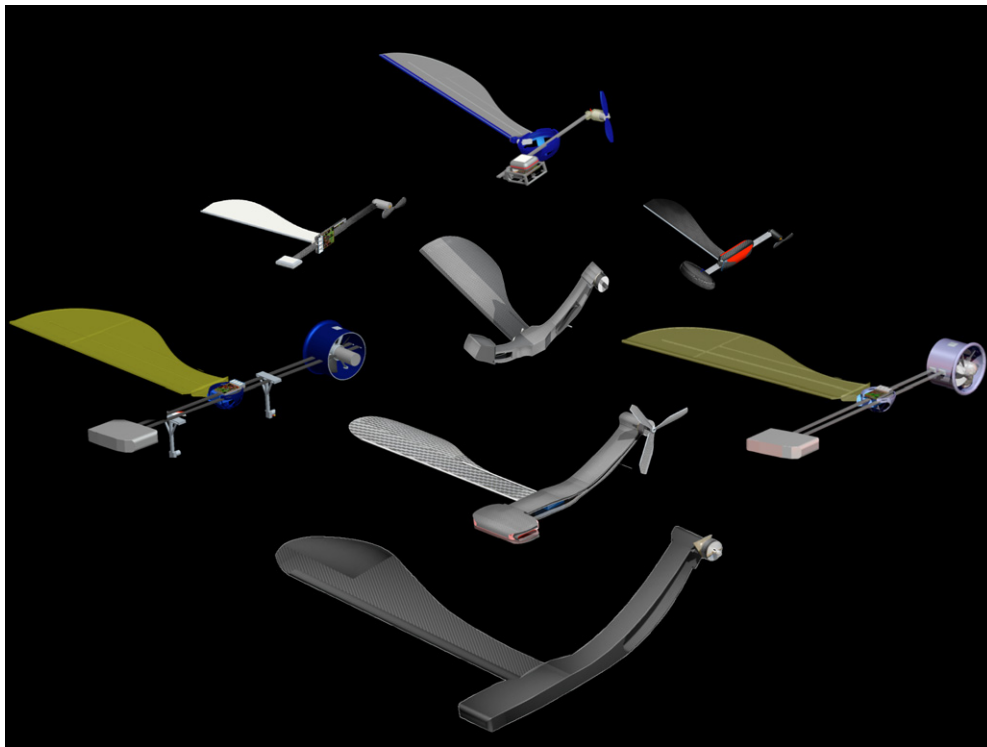


**Figure 14.** Design iterations of the robotic samara (not to scale).

event of motor failure, the vehicles gently autorotate back to the ground.

#### 4.2. Vehicle design

The unconventional wing and body structure are the result of an iterative design process which has produced on the order of 100 vehicles, several of which are shown in figure 14. The resultant vehicles are extremely damage tolerant as they employ flexible structures which deflect upon impact, effectively increasing the time over which the impact load is applied to the vehicle. The configuration of the vehicles is shown in figure 12. Advantages over traditional micro-scaled vertical take-off and landing (VTOL) configurations include passive stability [11],

efficient autorotation [10], low fuselage drag, mechanical simplicity, low cost, high payload capacity and substantial damage tolerance.

**4.2.1. Structures.** The primary load-bearing structure of the vehicle is 0/90 ply 0.025 inch thick carbon-fiber composite laminate, with opposed parallel tension and compression members mounted to the motor and wing. In this configuration, the structure provides a high degree of flexure in the  $\hat{z}$ -direction and a high degree of stiffness in the plane of rotation. The angle at which the motor is held provides protection from ground impingement on take-off and landing, figures 12 and 13.

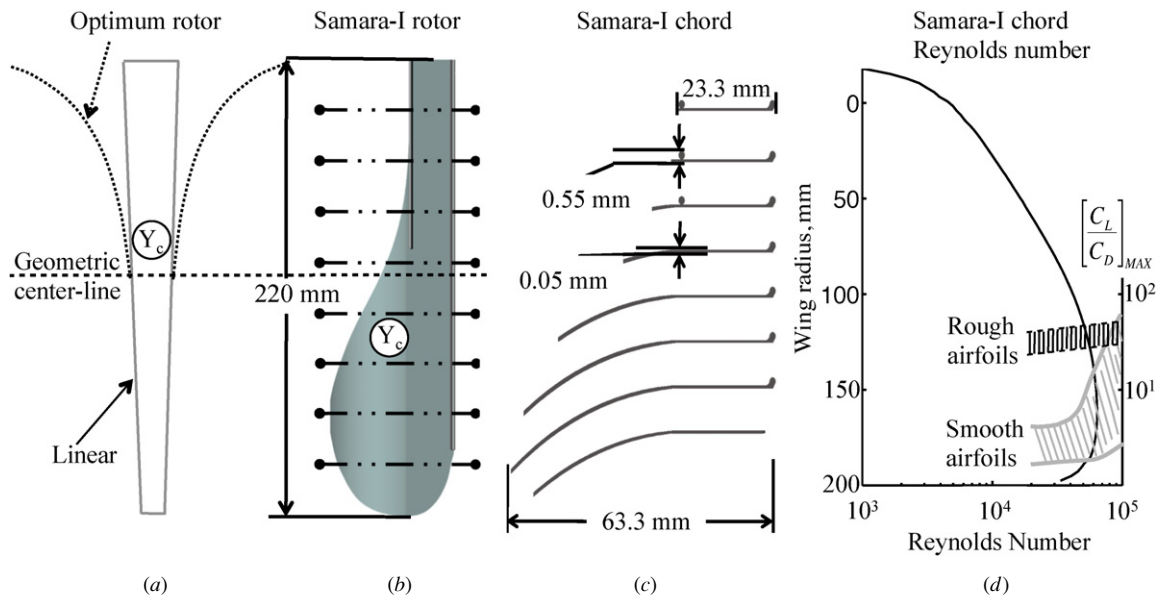


**Figure 15.** (a) Optimum helicopter rotor design, [21]. (b) Samara-I wing geometry and (c) Samara-I wing chord distribution. (d) Reynolds number variation with wing radius, [22].

**4.2.2. Power and propulsion.** Flight time of the samara-I is roughly 20 min with a 25 g, 480 mAh 7.4 V two-cell lithium-polymer (LiPo) battery, for a total vehicle mass (GW) of 75 g. The maximum gross take-off weight (GTOW) of the vehicle is 125 g, and the maximum dimension is 270 mm. The second and smaller samara tested called samara-II is designed and constructed in a similar fashion to samara-I. However, the total mass is 38 g, and the maximum dimension is 180 mm, figure 13. The smallest of the robotic samaras has a maximum dimension of 75 mm; samara-III is powered by a 60 mAh 3.4 V single-cell LiPo battery and has a maximum flight time of > 2 min. This vehicle has a passive flap hinge and does not have servo control collective pitch, which reduces control to the vertical axis. Tables 7, 8 details the mass breakdown of samara-I, II, III.

**4.2.3. Payload and mass fractions.** Pines and Bohorquez [16] found the propulsion system of small-scale fliers typically exceed 60% of the total vehicle mass, compared to a jetliner which boasts a propulsion system with a 40% mass fraction. 20% savings at full scale is used entirely for payload as the Boeing 767 payload mass fraction is 29%, compared to 9% for small-scale flight vehicles, table 8. The mass fractions of the propulsion system of samara-I, II without payload are 47% and 42% respectively, table 7. If we consider the vehicles maximum GTOW for this calculation, the mass fractions of the propulsion system drop to 28% and 35%, respectively, with payload fractions of 40% and 21%, table 8.

**4.2.4. Wing design.** The aerodynamics of the robotic samara is subject to the scaling of Reynolds number  $Re$ , which is the ratio of inertial to viscous forces, and is a measure of the flow conditions over a body immersed in a fluid. The importance of this relationship as applies to biological/bio-inspired systems can be understood through Nachtigall's [20] postulate of the

**Table 7.** Size and performance of robotic samara-I, II, III.

Robotic samara	I	II	III
Mass (g)	75	38	9.5
Max GTOW (g)	125	48	10.5
Max dimension (mm)	270	180	75
Payload	0	0	0
Flight time	20 min	10 min	> 2 min
Propeller	5.3	2.6	4.2
Tailboom	2.6	3.3	3.0
Motor	10.5	10.7	30.5
Wing/structure	26.3	27.6	24.4
Landing gear	2.6	2.7	2.0
Control system	18.4	16.0	6.0
Avionics	7.9	4.0	6.6
LiPo battery	26.3	33.3	23.2

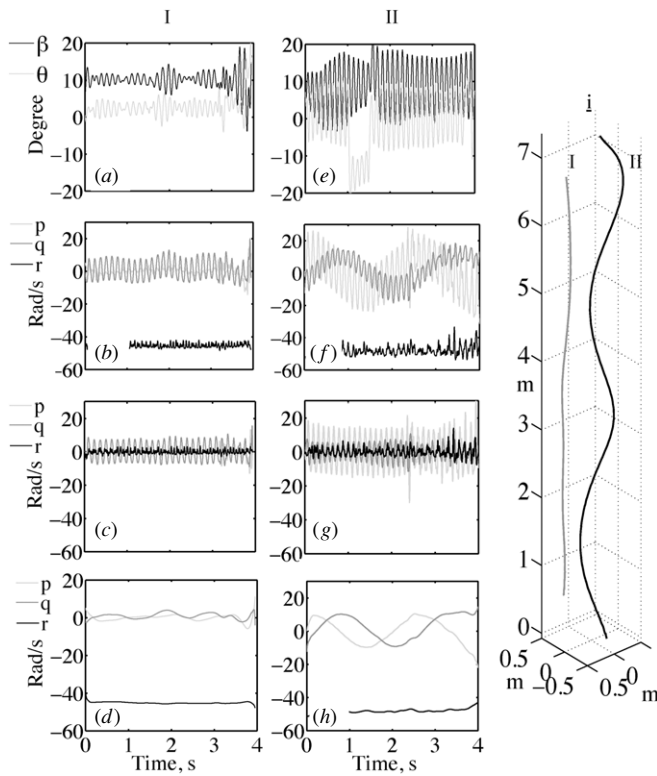
subcategories into which biological creatures flow properties can be grouped.

Relevant to this work, the second regime is inhabited by insects and small birds which use vortices to stay aloft and move through a fluid. This regime is presently poorly understood, as compared to the third regime that is dominated by inertial effects, and is the environment in which MAV's reside. To achieve peak performance it is desirable to have the lifting surface of a wing operate at its maximum lift-to-drag ratio ( $L/D$ ) as this is a measure of the wing's aerodynamic efficiency. The factors which determine  $L/D$  include wing geometry and surface roughness which influences the flow conditions over a given airfoil.

First observed by Schmitz [13], McMasters and Henderson [22] found the maximum  $L/D$  performance of various airfoils versus Reynolds numbers dramatically changed above  $Re = 70\,000$  for smooth airfoils, whereas rough airfoils exhibited a steady increase with the Reynolds number and out-performed smooth airfoils below  $Re = 10^5$ , figure 15(d). The variation of the Reynolds number with span

**Table 8.** Weight data (in terms of percent of GW).

Robotic samara (UMD)	I	II	III	Black Widow [17] (Aeronvironment)	MICOR [18] (UMD)	Microbat (Caltech)	Boeing 767
Gross weight	GW	GW	GW	GW	GW	GW	GW
Structure	20	25	26	18	12	24	35
Fuel/Propulsion	28	33	52	64	70	58	39
Avionics	12	21	12	9	9	18	9
Payload	40	21	10	9	9	0	17


**Figure 16.** Mechanical samara flight path, roll, pitch and yaw for modes I and II.

length for a robotic samara crosses this performance boundary at the out-board section of the wing, figure 15(d). It is therefore advantageous to distribute the wing area such that the largest chord sections are collocated with the largest Reynolds number thereby increasing the maximum  $L/D$  for that wing section, figure 15(b). This approach is as well based on findings from the autorotation experiments which indicated that an increase in the distance of the area centroid  $Y_c$  from the center of rotation leads to an increase in the efficiency of the wing which is measured by the descent rate [10]. Though the drag on inboard section of the vehicle/wing has not been quantified, the most substantial effect on performance is realized through increased wing length where an additional 10% can add up to 5 min of flight time to samara-I.

This approach differs from full-scale rotor design which seeks to minimize power losses by creating uniform inflow over the rotor disk [21]. This approach results in a rotor with large chord sections at a high angles of attack, close to the center of rotation, and small chord sections at lower angles of attack farther from the center of rotation, figure 15(a). The optimum

rotor blade at full scale has a hyperbolic radial distribution of blade chord; however, in practice a linear approximation is used and is beneficial to hovering rotor performance, figure 15(a). The blade twist shown in figure 15(c) helps with hover stability of the vehicle, however the total effect has not been quantified.

## 5. Stability properties

A substantial advantage of the samara-I, II vehicle is that it is a passively stable system. A simple qualitative stability analysis of the samara-I in a steady hover or autorotation illustrates this point. In a steady hover the thrust from the propeller ( $F_p$ ) is balanced by the drag from the body and wing ( $F_{Dw}$ ), resulting in a near-constant rotational rate about its principal inertial axis,  $I_z$ . The vertical force generated by the wing ( $F_{Lw}$ ) opposes the force of gravity ( $F_G$ ) resulting in a net zero vertical velocity. Alternatively, in autorotation, the resistive torque of the wing drag is equal to the driving torque of the lift, resulting in a net zero torque and vertical acceleration. Consider the assumed motion  $r = r_0$  and  $p, q \ll r_0$  in steady hover, or autorotation. To investigate whether the motion is stable or not, neglecting aerodynamic contributions, a small moment is applied to the body such that after the moment is applied the resultant angular velocities are as follows:

$$p = \epsilon_p \quad (23)$$

$$q = \epsilon_q \quad (24)$$

$$r = r_0 + \epsilon_r \quad (25)$$

where  $\epsilon_i$  ( $i = 1, 2, 3$ ) are infinitesimal quantities. To determine the evolution of these perturbed angular velocities in time, it is convenient to use the Euler equations as follows:

$$I_z(\dot{r}_0 + \dot{\epsilon}_r) + (I_x - I_y)\epsilon_p\epsilon_q = 0 \quad (26)$$

$$I_x\dot{\epsilon}_p - (I_y - I_z)(r_0 + \epsilon_r)\epsilon_q = 0 \quad (27)$$

$$I_y\dot{\epsilon}_q - (I_z - I_x)(r_0 + \epsilon_r)\epsilon_p = 0. \quad (28)$$

The change in angular velocities is small, and as such allows the linearization of the above equations by eliminating quadratic and higher order terms in  $\epsilon_i$  yielding

$$I_z\dot{\epsilon}_r = 0 \quad (29)$$

$$I_x\dot{\epsilon}_p - (I_y - I_z)r_0\epsilon_q = 0 \quad (30)$$

$$I_y\dot{\epsilon}_q - (I_z - I_x)r_0\epsilon_p = 0. \quad (31)$$



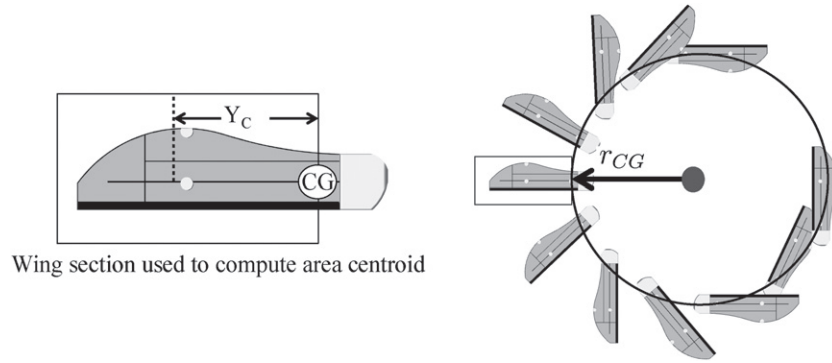


**Figure 17.** Area of wing used to compute  $Y_C$ . Also shown is the definition of the radius of precession of the center of mass ( $r_{CG}$ ) [10].

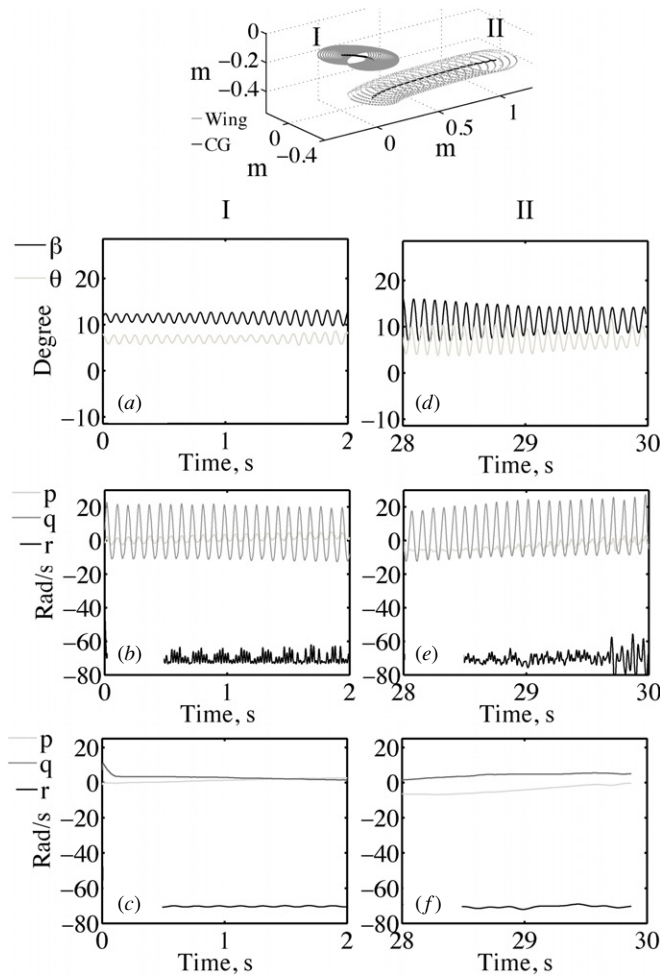


**Figure 18.** Flight test data for two different flight paths traversed by samara-I.

This implies  $\epsilon_r$  is constant. The behavior of the remaining angular velocities can be understood with eigenvalue analysis. Assuming a solution of the form

$$\epsilon_p(t) = E_p e^{\lambda t} \quad (32)$$

$$\epsilon_q(t) = E_q e^{\lambda t}. \quad (33)$$

Next, we can introduce the expansions into the linearized equations:

$$\begin{bmatrix} I_x \lambda & (I_z - I_y) r_0 \\ (I_x - I_z) r_0 & I_y \lambda \end{bmatrix} \begin{bmatrix} E_p \\ E_q \end{bmatrix} e^{\lambda t} = \begin{bmatrix} 0 \\ 0 \end{bmatrix}. \quad (34)$$

The solution requires the determinant of the coefficient matrix to be zero, yielding the characteristic equation

$$I_x I_y \lambda^2 - (I_x - I_z)(I_z - I_y) r_0^2 = 0. \quad (35)$$

The solution is

$$\lambda = \pm i \sqrt{\frac{(I_x - I_z)(I_z - I_y) r_0^2}{I_x I_y}}. \quad (36)$$

Two types of solutions are possible and depend on the principal moments of inertia. If  $I_x > I_z$  and  $I_y > I_z$ , or if  $I_x < I_z$  and  $I_y < I_z$  (characteristic of samara-I and samara-II) both roots of the characteristic equation are imaginary. In the absence of nonconservative forces, the system is marginally stable [29]. The inertial parameters of the samara vehicles as well as the resultant eigenvalues are listed in table 9.

## 6. Flight test

### 6.1. Observations from free-flight test

The second mode observed traced a 0.5 m diameter circle upon descent, whereas the first mode settled to trace a circle with diameter equal to 0.06 m. The two flight modalities identified, shown in figure 16(i), have been observed on all scale models tested. The first mode was the most frequently observed; however, the number of test conducted was not enough to quantify in a statistically meaningful way. The major differences found between the modes include mean feathering/coning angles, radius of precession and descent velocity. The coning and feathering angles from mode I averaged  $\bar{\beta} = 10.1^\circ$  with  $\sigma_\beta = 1.6^\circ$ , and  $\bar{\theta} = 2.4^\circ$  with  $\sigma_\theta = 1.8^\circ$ , figure 16(a). Flight mode II exhibited larger oscillations in coning and feathering with  $\bar{\beta} = 8.6^\circ$  with  $\sigma_\beta = 6.1^\circ$ , and  $\bar{\theta} = 1.3^\circ$  with  $\sigma_\theta = 7.4^\circ$ , figure 16(b).

The body angular velocities were found to be substantial and varying by as much as  $20 \text{ rad s}^{-1}$  in the roll ( $p$ ) and pitch ( $q$ ) axes, figures 16(b) and (f). Roll, pitch and yaw for both flight modes display cyclic (once per revolution) and low frequency ( $< 1 \text{ Hz}$ ) oscillations. Shown in figures 16(c)

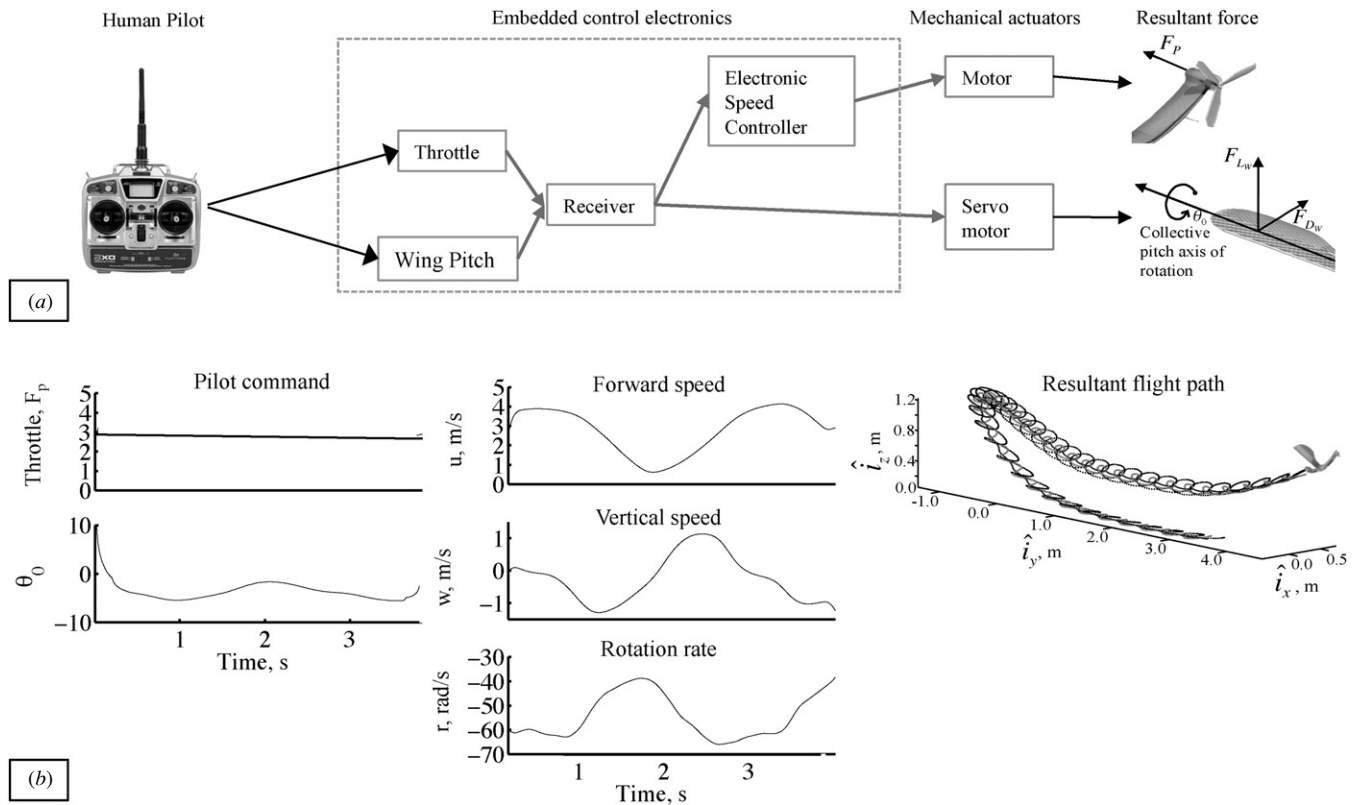


**Figure 19.** (a) Samara-I control synthesis and signal diagram. (b) Samara-I coordinated U-turn maneuver with corresponding control input and resultant vehicle dynamics and flight path, [12].

**Table 9.** Inertia properties, rotation rate and resultant eigenvalues for robotic samara-I, II.

	$I_x$ Kg mm <sup>2</sup>	$I_y$ Kg mm <sup>2</sup>	$I_z$ Kg mm <sup>2</sup>	$r_0$ rad s <sup>-1</sup>	$\lambda$
Samara-I	248	562	797	80.5	$\pm 0 + 77i$ rad s <sup>-1</sup>
Samara-II	35	98	122	76	$\pm 0 + 59i$ rad s <sup>-1</sup>

and (g) is the oscillatory excitation of ( $p, q, r$ ) that occurs near the rotational frequency  $r$ , and shown in figures 16(d) and (h) is the low frequency excitation that occurs at 0.7 Hz for the first mode I and 0.4 Hz for the second mode II.

## 6.2. Observations from powered flight test

Controlled flight of the robotic samara platform demonstrated the similarities between the unpowered/powered rigid body dynamics. The two modes of flight observed in unpowered flight are evident in powered flight, where the change in the radius of precession is used to dynamically steer the vehicle to a desired location. The two tests shown in figure 18 are for flight paths which carve out different size circles. The coning and feathering angles differ in magnitude and can be seen to result from the roll, pitch and yaw body rates. The body angular rates for both turns are shown in figures 18(b) and (e), and the mean angular rates are shown in figures 18(c) and (f). Larger oscillations can be seen in  $\beta, \theta$  for the path which carves out a larger circle, as was the case for the unpowered samara.

Control of the vehicle is done through open loop piloting, where the path of the signal from pilot to robotic samara is shown in figure 19(a). Lateral directional flight was recorded in the laboratory for a flight path consisting of an initial trim state and a perturbation about the trim, figure 19(b). In general, the turn radius is inversely proportional to the collective pitch of the wing. While an impulsive input changes the heave velocity of the vehicle, a step input changes the turn radius of the flight path. The samara travels in the opposite direction of the motion that would be induced by an impulsive collective input applied at that instant. The finding that the step response spends part of its time going in the wrong direction is an indication of a nonminimum phase system, or a right-half-plane zero, and the vehicle's differing responses to impulsive and step inputs are leveraged to create a control strategy that provides full controllability, where an alternating series of large and small turn radii can be used to steer the vehicle in a specific direction. While a right-half-plane zero is normally a performance limitation, in this case the behavior that typically restricts the performance has been used in the control strategy to enable a single input to control multiple degrees of freedom, [12]. The range of the samara-I vehicle is 4.8 km which is



**Figure 20.** Smallest robotic samara constructed.

computed using its maximum translational velocity for 20 min of flight.

The velocity components and rotation rate are shown in figure 19(b) as they vary with the input  $\theta_0$ . The first 0.5 s of flight correspond to a near constant  $u$  and near zero  $w$ . At the time of the U-turn, 1–1.5 s, there is an increase in the vertical velocity. The increase is correlated because a collective pitch increase used to change the heave velocity is also used to change the flight path direction.

Compared to hover, forward flight is more efficient for rotary-winged vehicles as the wind velocity incident on the wing is larger, resulting in a higher  $L/D$ , [21]. Samara-I has a rotation rate and wing radius that correspond to a hover tip velocity of roughly  $14 \text{ m s}^{-1}$ , at 50% span  $7 \text{ m s}^{-1}$ , and 25% span  $3.5 \text{ m s}^{-1}$ . A forward velocity greater than  $3.5 \text{ m s}^{-1}$  would cause flow reversal on the inboard 25% of the wing; however, the majority of the vertical force is located on the outboard 50% of the wing, for which flow reversal may occur above  $14 \text{ m s}^{-1}$ . The vehicle has been observed to move forward at a maximum velocity of  $4 \text{ m s}^{-1}$ , which may result in flow reversal on the inboard 25% of the wing. This will degrade performance at this section of the wing and will result in a tilting of the tip path plane, as the lift production is higher on the advancing side and lower on the retreating side.

**6.2.1. Scaling effects.** The flight dynamics observed in the passive and robotic samara have been found to exist in both larger and smaller prototypes ranging from 0.5 to 0.075 m. The smallest and lightest robotic samara constructed to date is shown in figure 20, where the wing of the vehicle is similar in size to a natural samara wing.

## 7. Conclusion

The work presented introduces a simple experimental methodology designed to decrease errors in the quantification of the flight dynamics of mechanical and robotic samara. The experiments presented strived for repeatability so that the observed dynamics were not artifacts of an unknown testing environment. The two modes of flight observed in autorotating mechanical samaras provided the inspiration for the design of

a control system for a powered robotic samara that does not require high frequency sensing and actuation typical of micro-scaled rotorcraft.

The flight modalities identified differ in descent velocity, coning/feathering angle as well as roll, pitch and yaw rate. It was found that active control of the feathering angle allowed the variation of the radius of the helix carved by the samara upon descent. This knowledge was used to design a hovering robotic samara capable of lateral motion through a series of different size circles specified by precise actuation of the feathering angle. Inspection of the flight dynamics reveals substantial similarities in the behavior of the passive descending samara and the powered robotic samara. This is of interest to those studying population dynamics of samara-bearing trees as it provides a low cost platform with a derived flight dynamics model which can facilitate future testing of samara reaction to horizontal winds. It also provides a platform for the testing of various wing efficiencies, as the wing is interchangeable and can be used to measure the power required to hover for a given geometry. This study as well brings insight into the study of natural samara, as precise flight test data were presented for fabricated samaras revealing flight modalities that may play a role in population dynamics.

## Acknowledgments

Thanks to the Faculty and staff of the University of Maryland for so graciously providing the facilities for these experiments. Thanks to the Autonomous Vehicle Laboratory, and the Alfred Gessow Rotorcraft Center for their continued teamwork and inspiration. This work was supported by the ARO MURI grant and the A James Clark School of Engineering, University of Maryland.

## References

- [1] Azuma A 1992 *The Biokinetics of Flying and Swimming* (Tokyo: Springer) pp 105–121
- [2] Azuma A and Yasuda K 1997 The autorotation boundary of the flight of samaras *J. Theor. Biol.* **185** 313–20
- [3] Seter D and Rosen A 1992 Stability of the vertical autorotation of a single-winged samara *J. Appl. Mech.* **59** 1000
- [4] Seter D and Rosen A 1991 Vertical autorotation of a single-winged samara *J. Appl. Mech.* 1000–8
- [5] Norberg R A 1973 Autorotation, self-stability, and structure of single-winged fruits and seeds (samaras) with comparative remarks on animal flight *Biol. Rev.* **48** 561–96
- [6] Green D S 1980 The terminal velocity and dispersal of spinning samaras *Am. J. Bot.* **67** 1218–24
- [7] Lentink D *et al* 2009 Leading-edge vortices elevate lift of autorotating plant seeds *Science* **324** 1438
- [8] Pirie M D, Klitgaard B B and Pennington R T 2009 Revision and biogeography of *Centrolabium* (Leguminosae–Papilionoideae) *Systematic Bot.* **34** 345–59
- [9] Ulrich E, Pines D and Park J 2009 Mechanical samara deployment and passive distribution by a fixed wing unmanned air vehicle *AHS Int. Specialist Meeting on Unmanned Rotorcraft*, (Phoenix, AZ, Jan. 2009)
- [10] Ulrich E and Pines D 2010 Effects of planform geometry on mechanical samara autorotation efficiency and rotational dynamics *J. Am. Helicopter Soc.* in press

- [11] Ulrich E, Pines D and Humbert J S 2010 Pitch and heave control of robotic samara micro-air-vehicles *J. Aircr.* **47** 1290–9
- [12] Ulrich E, Faruque I, Grauer J, Pines D, Humbert J S and Hubbard J 2010 Control model for robotic samara: dynamics about a coordinated helical turn *J. Guid. Control Dyn.* **33** 1921–6
- [13] Schmitz F W 1942 *Aerodynamik des flugmodells* (Berlin: C.J.E. Volckmann Nachf. E. Wette)
- [14] Graham F 1999 *Monocopters* (East Liverpool, OH: Perigee Press)
- [15] Jameson S, Allen N and Youngren H 2007 SAMARA I Nano Air Vehicle—A Revolution in Flight. DARPA Contract W31P4Q-06-C-0324
- [16] Pines D and Bohorquez F 2006 Challenges facing future micro-air-vehicle development *J. Aircr.* **43** 290–305
- [17] Grasmeyer J *et al* 2001 Development of the Black Widow Micro Air Vehicle *AIAA Paper* 2001-0127 39th Aerospace Sciences Meeting and Exhibit (Reno, NV, 8–11 January 2001)
- [18] Samuel P, Sirohi J, Rudd L, Pines D and Perel R 2000 Design and development of a micro coaxial rotorcraft *Proc. AHS Vertical Lift Aircraft Design Conf.* (Alexandria, VA, Jan. 2009)
- [19] Stevens B L and Lewis F L 2003 *Aircraft Control and Simulation* (Hoboken, NJ: Wiley) pp 25–7
- [20] Brodsky A K 1994 *The Evolution of Insect Flight* (New York: Oxford University Press) p 51
- [21] Leishman J G 2006 *Principals of Helicopter Aerodynamics* (Cambridge: Cambridge University Press)
- [22] McMasters J H and Henderson M L 1980 Low Speed Single Element Airfoil Synthesis *Tech. Soaring* **6** 121
- [23] [http://www.objet.com/3D-Printer/Eden350\\_Eden350V/](http://www.objet.com/3D-Printer/Eden350_Eden350V/)
- [24] [http://www.objet.com/Docs/FullCure\\_3D%20Modeling\\_Letter.pdf](http://www.objet.com/Docs/FullCure_3D%20Modeling_Letter.pdf)
- [25] [http://www.vicon.com/\\_pdfs/t\\_cameras.pdf](http://www.vicon.com/_pdfs/t_cameras.pdf)
- [26] Hochmann D and Sadok M 2004 Theory of synchronous averaging *IEEE Aerospace Conf. Proc., Institute for Electrical and Electronics Engineers* pp 3636–53
- [27] Samuel P and Pines D 2003 *Helicopter transmission diagnostics using constrained adaptive lifting* *AHS 59th Annu. Forum Proc.* Phoenix, AZ, May 2003
- [28] Klein V and Morelli E 2006 *Aircraft System Identification: Theory and Practice (AIAA Education Series)* (Reston, VA: AIAA) chapter 4
- [29] Baruh H 1999 *Analytical Dynamics* (New York: McGraw-Hill)